System Design and Control of Anthropomorphic Walking Robot *LOLA*

Sebastian Lohmeier, Thomas Buschmann, and Heinz Ulbrich

***Abstract*—This paper presents the 25-DOF full-size humanoid robot *LOLA*. Our goal is to realize fast and human-like walking. Furthermore, we want to increase the robot's autonomous, vision-guided walking capabilities. *LOLA* is characterized by a redundant kinematic configuration, an extremely lightweight design, joint actuators with brushless motors and an electronics architecture using decentralized joint control. Special emphasis was put on an improved mass distribution to achieve good dynamic performance. Center of mass trajectories are calculated in real-time from footstep locations using a spline collocation method. Reference trajectories are modified by a stabilizing control system based on hybrid force/position control with an inner joint position control loop.**

***Index Terms*—Anthropomorphic robots, humanoid robots, legged locomotion, robot design, robot dynamics, walking control.**

I. Introduction

According to a recent paper on the robotics market, humanoid service robots might be an emerging application area [1]. The anthropomorphic structure is one reason why such systems are ideal general-purpose assistant robots for typical everyday tasks. Other scenarios include the entertainment industry and academic education and research.

Quite a few sophisticated full-size humanoid robots are developed by companies, like Toyota's running robot [2] and Honda's *ASIMO* [3], while most are developed by research laboratories and universities, for example, *H7* [4], *HRP-2* [5] and *HRP-3* [6] (AIST and Kawada Industries), *WABIAN-2* [7], *HUBO* [8], and *JOHNNIE* [9].

For everyday tasks in production, office or home environments, stable and fast biped locomotion is a basic skill. Compared with human beings, higher walking speeds, and flexible motion generation still remain challenging due to many unsolved control problems, e.g., fast walking and running [2], [10], sudden turning motions, walking on rough terrain and trajectory generation in complex environments. On the other hand, the robot hardware contributes significantly to system performance if designed thoroughly: both robot hardware and software must be seen as tightly coupled parts of a highly integrated mechatronic system.

The first part of this paper gives an overview of the mechatronic system: the fundamental design considerations and key components of the mechanical design are presented. The second part deals with the robot simulation, and outlines the real-time trajectory generation and stabilizing control.

Manuscript received February 13, 2009; revised July 1, 2009. First published October 9, 2009; current version published November 11, 2009. Recommended by Guest Editor M. Goldfarb. This work was supported by the Deutsche Forschungsgemeinschaft under Grant UL 105/29.

The authors are with the Institute of Applied Mechanics, Technical University Munich, 85748 Garching, Germany (e-mail: lohmeier@amm.mw.tum.de; buschmann@amm.mw.tum.de; ulbrich@amm.mw.tum.de).

Color versions of one or more of the figures in this paper are available online at http://ieeexplore.ieee.org.

Digital Object Identifier 10.1109/TMECH.2009.2032079

Fig. 1. Photograph of the 25-DOF humanoid walking robot *LOLA*.

TABLE I
Hardware Specification

General	Height	[illegible]
	Weight	[illegible]
	Total DOF	[illegible]
	Maximum Walking Speed (estimated)	[illegible]
	Power supply	external
Legs	DOF (hip: [illegible], knee: 1, ankle: [illegible])	[illegible]
	Thigh length	[illegible]
	Shank length	[illegible]
	Foot height	[illegible]
	Distance between hip joints	[illegible]

II. System Overview

LOLA is 180 cm tall and weighs approximately 55 kg. The physical dimensions of the robot are based on anthropometric data. Fig. 1 shows a photograph of the robot, the key data are summarized in Table I. The distinguishing characteristics of *LOLA* are the redundant kinematic structure with 7-DOF legs, an extremely lightweight construction, and a modular joint design with high power density based on brushless motors. The mass distribution of the legs is improved to achieve good dynamic performance.

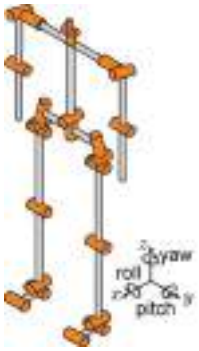

Joint	DoF
Head	3
Shoulder	2
Elbow	1
Pelvis	2
Hip	3
Knee	1
Ankle	2
Toe	1
Total	**25**

Fig. 2. Kinematic structure of *LOLA*.

A. Kinematic Structure

Simulations and experiments have shown that additional, redundant DOFs enable more natural and flexible gait patterns and extend the abilities of the robot in general. Fig. 2 shows the kinematic configuration with 25 actuated DOFs: the legs have 7 DOFs each, the pelvis has 2 and each arm has 3 DOFs. The 3-DOF stereo camera head consists of a pan/tilt unit. In addition, the angle of convergence can be adjusted, enabling stereo vision of objects close to the robot.

Considering the leg and pelvis joints, the kinematic chain of the upper body with respect to the stance foot has a redundant structure with 9 DOFs. Kinematic redundancies augment the robot's agility, but they also contribute to reducing joint loads.

LOLA has active toe joints that allow to control the center of pressure during heel rise, whereas robots with monolithic feet or passive toe joints would be marginally stable. Area contact of the toe segment stabilizes the robot and facilitates forward roll across the forefoot. Moreover, heel lift-off during terminal stance, which occurs shortly before the swing leg contacts the ground, can also reduce joint loads. As found by Kerrigan *et al.* [11], heel rise in human gait contributes significantly to reducing the center of mass (CoM) vertical displacement. Due to the importance of stance leg heel rise in human walking, the idea of implementing toe joints on a humanoid robot is not new. Yet, there are very few humanoid robots with actively driven toe joints, e.g., [2], [12].

B. Sensor System

The sensor system supports the implementation of model-based control algorithms and is optimized for signal quality and bandwidth.

1) Joint Sensors: Absolute angular sensors on the output shafts of all joints compensate elasticities and nonlinearities in the drivetrains and enable the robot to (theoretically) start from arbitrary positions. We use Heidenhain EnDat interface (ECI) encoders with a resolution of 17 bit and an accuracy of 0.1°, which are used as a resolver replacement in industrial motor control. The cutoff frequency is 6 kHz and the latency for continuous sampling of position values is 5 μs. Thus, the delay in position feedback is minimal and the velocity measurement can be done by numerical differentiation.

2) Force/Torque Sensors: Two custom-made six-axis force/torque sensors are tightly integrated into the foot structure. The sensor body is a monolithic aluminum component with four shear beams in a Maltese cross arrangement. Each beam holds two pairs of strain gauges connected to half bridges. Thin membranes decouple the beam deflections to a far extent and reduce crosstalk. In order to protect the sensor from damage during experiments, mechanical end stops are integrated as an overload protection. A calibration error of less than 0.5% is achieved by applying many different load cases. At a total weight of 395 g the sensor includes an overload protection and all necessary electronics.

3) Inertial Measurement Unit (IMU): The IMU estimates the orientation and angular velocities of the upper body. Since accuracy and signal quality of the IMU considerably affect the performance of the stabilizing controller, we have chosen a commercial high-precision IMU (iVRU-FC-C167, iMAR Navigation) with fiber-optic gyroscopes and MEMS accelerometers.

III. Mechatronic Design Concept

LOLA's hardware approach is based on experiments with *JOHNNIE* and tries to settle most of the technical problems discovered during a thorough hardware analysis. The fundamental design concept is inspired by research on human walking and the underlying mechanisms. State-of-the-art mechatronics technology is used to create a highly dynamic robot with enhanced walking capabilities and autonomy.

A. Design Process

Fast locomotion poses a significant challenge for biped robots and requires a thorough design of the mechatronic system. The robot development follows the procedure described in guideline VDI 2206 "Design methodology for mechatronic systems" [13]. It is an iterative and open-ended process of design and simulation.

After certain design milestones have been completed, new inertia properties of the links and actuators are obtained from the 3-D-computer-aided design (CAD) model. These are used to calculate joint loads, workspaces and constraint forces using the dynamics simulation of the robot (Section VI), which are the basis for the dimensioning of actuators and structural components. In this way, both simulation and CAD model are iteratively refined.

B. Special Requirements for High-Speed Walking

Without doubt, many open questions make the control of fast walking very challenging. Increased robustness and flexibility are key components to guarantee stability of the robot in different situations. This is achieved by an integrated control approach which combines the stabilization of global dynamics by manipulation of contact forces and hybrid force/position control in task space (Section VIII). Fast walking also requires an improved real-time walking pattern generation. A new method is used to calculate the reference trajectories for the following three steps (Section VII).

Moreover, several aspects in the design of the mechanical system can improve system performance. Besides a revised kinematic structure, three design objectives are defined to improve leg dynamics: 1) sufficient mechanical stiffness; 2) high CoM; and 3) low moments of inertia of the leg links.

C. Design Features to Improve System Dynamics

1) Mechanical Stiffness: Both static and dynamic behaviors of the mechanical system have a strong influence on the walking capabilities. In particular, structural weak points of the locomotor system can degrade walking performance by causing structural vibrations and deviations from the reference trajectories, which can destabilize the robot.

The basic design objective is, therefore, to balance structural stiffness and actuator performance with lightness of the mechanical parts. To avoid a particular range of resonant frequencies, these considerations cannot be limited to the component-level. Rather, the elastodynamic dimensioning of the robot structure must include the drivetrains and other components within the load path, such as bolted flange connections and link bearings. For instance, stiffness-based gear selection is carried out in addition to the "standard" procedure of torque-speed-based dimensioning in order to minimize oscillations of the feet. With the torsional stiffness K of the gear and an effective moment of inertia J, the resonance frequency at the gear output is

$$f = \frac{1}{2\pi}\sqrt{\frac{K}{J}}\,. \tag{1}$$

As an empirical value recommended by the gear manufacturer, f should be above 15 Hz.

2) CoM Height: Unlike humans, the largest portion of a biped robot's weight resides in its legs, since motors and gears determine approximately a third of the overall weight. The CoM height is therefore lower than in humans, typically at the height of the hip joint or below. According to the *linear inverted pendulum mode* by Kajita *et al.* [14], one possible solution for CoM lateral motion are pieces of hyperbolic curves

$$\Delta y_{\mathrm{CoM}} \propto \cosh\left(\sqrt{\frac{g}{z_{\mathrm{CoM}}}}\,T_s\right). \tag{2}$$

According to this model, the CoM lateral swing Δy_{CoM} decreases with higher CoM positions z_{CoM} for a given single support period T_s. Especially at higher walking speeds, the stability of the robot is increased if Δy_{CoM} is small, because of reduced oscillations of the angular momentum around the longitudinal axis. A more human-like mass distribution could be achieved by adding weight to the upper body, which would in turn require larger actuators and increase the weight of the leg segments. Our approach is therefore to shift the total CoM as close as possible to the hip joint while keeping the robot's overall weight minimal.

3) Leg Inertia: Mass distribution in the leg apparatus is a design variable which not only affects CoM position, rather, the influence on the inertia of individual leg segments is much more significant. Minimizing the resulting leg inertia and reducing its posture dependence is an important way of improving: 1) the dynamic performance of the system in general; 2) the accuracy of model simplifications; and 3) the performance of stabilizing control.

TABLE II
GEAR SIZES, REDUCTION RATIOS AND JOINT WORKING RANGES

Joint[a]		Gear		Torque	Speed	Workspace
		Type[b]	Ratio i	[Nm]	[rad/s]	[deg]
Hip	R	HD	[illegible]	281	8.16	−[illegible]
	P	HD	[illegible]	370	12.56	[illegible]
	Y	HD	[illegible]	281	8.16	[illegible]
Knee	P	RS	[illegible]	349	12.01	[illegible]
Ankle	R	RS	[illegible]	286	9.13	[illegible]
	P	RS	[illegible]	286	9.13	[illegible]
Toe	P	HD	[illegible]	84	12.56	[illegible]
Pelvis	R	HD	[illegible]	147	8.16	[illegible]
	Y	HD	[illegible]	147	8.16	[illegible]
Shoulder	P	HD	[illegible]	117	8.16	[illegible]
	R	HD	[illegible]	101	9.17	[illegible]
Elbow	P	HD	[illegible]	101	9.17	[illegible]
Head	Y	HD	[illegible]	9.7	8.9	[illegible]
	P	HD	[illegible]	14.0	15.5	[illegible]
	C	HD	[illegible]	20.9	15.5	[illegible]

[a]R = roll, P = pitch, Y = yaw, C = convergence.
[b]HD = Harmonic drive, RS = roller screw.

Our approach is to design major structural components as investment castings made from aluminum. In order to meet the weight and stiffness targets, design proposals are created by topology optimization [15]. Moreover, actuator performance is increased carefully (Section IV-A) and new kinematic structures are developed for the knee (Section IV-B) and ankle joints (Section IV-C), so that heavier component parts can be placed close to the hip joint axis.

IV. MECHANICAL DESIGN

A. Actuator Design

The joint actuators account for about a third of the total weight, making the development of compact and lightweight actuators crucial. We use high-performance permanent magnet synchronous motors (PMSM) because of their superior torque and speed capabilities. These motors allow to either increase actuator performance without adding additional weight, or decrease actuator mass without decreasing performance. The joints are driven through harmonic drive gears and planetary roller screws, respectively. Table II shows the gear sizes, reduction ratios, and working ranges of all joints. Further details on the actuator design have been published in [16].

B. Knee Joint

A harmonic drive-based actuator located in the knee joint axis would unacceptably increase the thigh moment of inertia, and a large part of the enhanced hip joint output would be spent on accelerating the heavier thigh. By employing a roller screw-based linear drive as shown in Fig. 3, mass distribution in the hip-thigh area is significantly improved: the motor is located close to the hip joint axis, reducing the thigh inertia by 65%, and the mass of the actuator itself by more than 10%, without reducing performance. The four-bar linkage mechanism

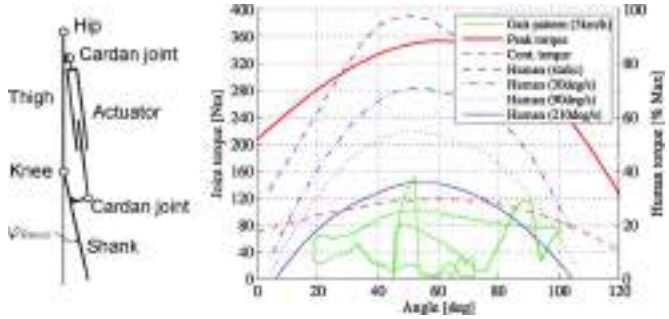

Fig. 3. Mechanism employed for the knee joint (left). Torque and speed requirements of knee joint, human torque capacity adapted from [17] (right).

is backlash-free, back-drivable and has a nonlinear torque-speed characteristic similar to the human knee (Fig. 3, right-hand side): the maximum torque occurs around 55°, which is advantageous for typical gait patterns. Conversely, maximum speeds increase at a stretched leg configuration where they are needed.

C. Ankle Joint

The ankle joint axes differ clearly in their torque-speed characteristics. By employing parallel drives, the motor peak torques can be reduced by about 35% [15]. Fig. 4 explains the functionality of the ankle joint actuation: the ankle joint (3) is actuated by two spatial slider-crank mechanisms (7)–(9) with 1 DOF each, where the motors (4) are mounted on the thigh (1), close to the hip joint. Compared to a previous design concept [15], the joint workspace is increased and shank inertia with respect to the hip joint is reduced by more than 20%.

Each linear drive is composed of a roller screw (8) mounted on the shank and a linear bearing (9) to keep the screw free from radial loads. The link (10) connects the linear carriage (7) and the foot segment. The synchronous belt (5) connects the motor shaft (4) to the input shaft of the bevel gear (6) in the knee joint axis. The output shaft of (6) finally drives the roller screw (8), which is arranged in longitudinal direction of the shank and perpendicular to the knee joint axis. The absolute angular sensors (11) allow direct measurement and control of the joint angles.

The planetary roller screws are preloaded and free from backlash. The whole mechanism is back-drivable.

The longer transmission distance reduces inertia and gravity loading. On the other hand, the spatial separation of electric motor and transmission requires the use of auxiliary transmissions and couplings, which may introduce elasticity and reduce system stiffness. To achieve high transmission accuracy without adding too much elasticity and backlash to the drivetrain, a synchronous belt (5) with a high tensile stregth and an optimized tooth profile is chosen. The bevel gear (6) is a commercial precision gear with minimal backlash ($\ll$8 arc min), optimized for position servo applications.

D. Foot Dynamics

During normal locomotion, the feet are the only parts of the robot which are subject to external loads. They are the last

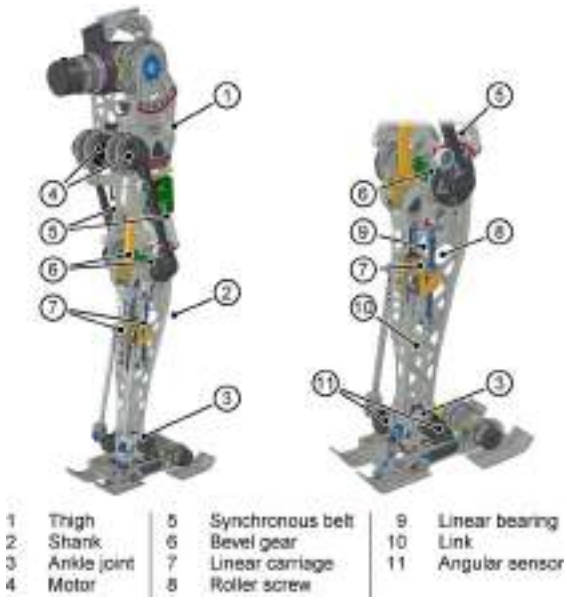

Fig. 4. Ankle joint actuation by a 2-DOF parallel mechanism.

segments of the leg kinematic chains and undergo the largest accelerations. The mechanical structure must, therefore, be extremely lightweight, yet it must be able to withstand shock loads of a multiple of the robot's weight during initial contact.

Despite the obvious fact that foot dynamics have a strong influence on the walking performance, there is surprisingly little detailed literature. Most robotic feet consist of a monolithic baseplate covered with rubber or plastic to increase friction and use compression/shear mounts as shock absorbers [3], [5]. Under shear loading, however, the stiffness of such elements is considerably lower than under pressure loading which can easily destabilize the robot during stance.

Developing a functional foot design is not trivial, thus, it is useful to take the main functions of the human foot into account. The main requirements are:

1) high grip on different surfaces, to ensure proper ground contact;
2) passively compliant elements with a) good damping characteristics for shock attenuation at initial contact and b) progressive spring characteristics at ground contact to ensure effectiveness of stabilizing control;
3) rigid mechanical structure to transmit propulsive forces at a bandwidth sufficient for system stabilization;
4) compensate smaller unevenness;
5) minimal weight.

From these requirements, the design of the robotic foot shown in Fig. 5 is derived. The toe joint (1) divides the foot into forefoot (2) and hallux (3). The force/torque sensor (4) is designed as an integral, load-bearing element within the forefoot. The modular mechanical configuration with the bolted flange connections (5) facilitates experiments with different foot geometries and allows to easily adjust the support polygon.

Several mechanisms are implemented for shock attenuation: viscoelastic layers (6) with good damping characteristics are used in analogy to the fat pads in the human heel and toe for

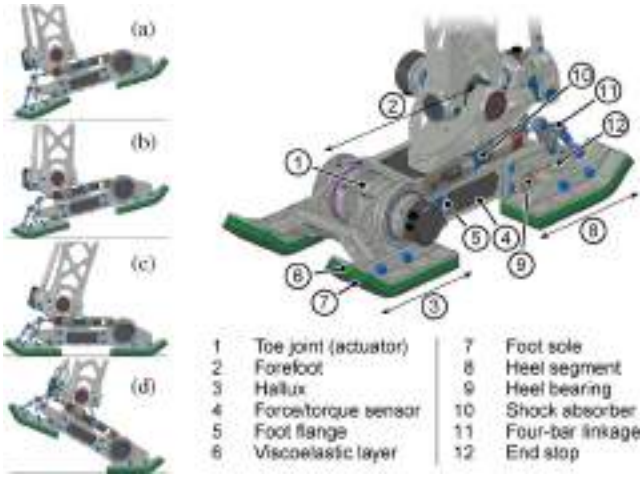

Fig. 5. Mechanical design of the feet: besides viscoelastic members, the passive heel segment with hydraulic damper contributes to shock attenuation.

damping the impact transients and compensating small unevenness. The foot sole (7) is made of wear-resistant, high-friction rubber. For improved energy dissipation during initial contact, a passive heel segment (8) similar to the human hindfoot and a hydraulic shock absorber (10) are implemented. The four-bar linkage (11) adjusts the strokes of heel and damper. The heel bearing (9) corresponds to the subtalar joint of the human foot [18]. The mechanical end stop (11) ensures the proper transmission of propulsive forces and stabilizing moments while in ground contact. The feasibility of the foot concept has been proved in preliminary tests with *JOHNNIE*.

The functionality of the foot in the different gait phases is illustrated in Fig. 5 (left): At initial contact (a) the heel segment protrudes from the foot sole. Its passive motion increases the time over which the foot is decelerated and during which energy is dissipated by the hydraulic damper. At loading response (b) the heel segment is retracted and more impact energy is dissipated by the deformation of the viscoelastic layer. Ground contact during midstance (c) is ensured by both heel and hallux, while the heel is lifted in terminal stance (d).

As in humans, passive and active mechanisms of shock absorption complement each other: the compliant contact elements and the heel damper act as a mechanical low-pass for the transferred forces. Although it is necessary to attenuate impact transients, compliance in the foot–ground contact bounds the mechanical bandwidth of transferable forces and moments. Passive shock absorption is therefore limited by the bandwidth required for stabilizing the upper body orientation and is complemented by active mechanisms, cf., Section VIII.

V. Electronics Architecture

Fig. 6 gives a schematic overview of the electronics architecture. *LOLA* is controlled by a central control unit (CCU) mounted on the upper body and nine local controllers carrying out low-level tasks, such as joint control and sensor data processing. Similar to hierarchical structures in biological systems, sensor data is preprocessed decentrally and only relevant information is forwarded to the CCU. Local controllers and CCU are connected via the Ethernet-based real-time communication system Sercos-III. The CCU is based on a PC platform (Core 2 Duo Mobile, 2.33 GHz), running the QNX real-time operating system. The local controllers are a custom development because of compactness and various sensor–actuator interfaces.

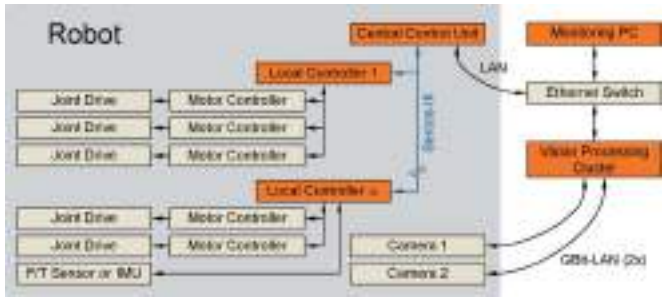

Fig. 6. Electronics architecture of *LOLA*.

Gait generation and stabilization run on the on-board computer system without any support from outside except for power supply. An external PC is used only for monitoring purposes and to give basic operating commands if the robot is not connected to the vision system. Due to high computing power requirements, vision processing is done on an external PC cluster.

VI. Dynamics Simulation

A key tool for hardware and controller design is a dynamics simulation for calculating loads, analyzing system dynamics, control system robustness, and performance. This section presents a refined version of the simulation system described in [19], which is used for developing and testing *LOLA*'s hardware and control algorithms. We model the robot as three coupled dynamical systems: 1) rigid multibody dynamics; 2) contact dynamics; and 3) drive dynamics.

A. Rigid Multibody Dynamics

The equations of motion (EoM) for the multibody system (MBS) are calculated recursively using the Newton–Euler method, exploiting the robot's tree structure to increase efficiency. The result is a set of nonlinear ordinary differential equations (ODEs) describing the rigid multibody dynamics

$$\boldsymbol{M}\ddot{\boldsymbol{q}} + \boldsymbol{h} = \boldsymbol{W}_{\lambda}\boldsymbol{\lambda} + \boldsymbol{W}_{\tau}\boldsymbol{\tau}. \tag{3}$$

Here, $\boldsymbol{M}$ is the mass matrix and $\boldsymbol{h}$ the vector of smooth forces. $\boldsymbol{\lambda}$ are the contact forces acting on the MBS via the Jacobian $\boldsymbol{W}_{\lambda}$, while $\boldsymbol{\tau}$ and $\boldsymbol{W}_{\tau}$ are the actuator forces and actuator force Jacobian, respectively.

B. Contact Dynamics

The robot contacts the ground with its feet which are equipped with compliant, shock absorbing materials (cf., Section IV-D). During walking the elastic contact elements are compressed by several millimeters, greatly influencing system dynamics. In simulation, these materials are modeled as linearly viscoelastic

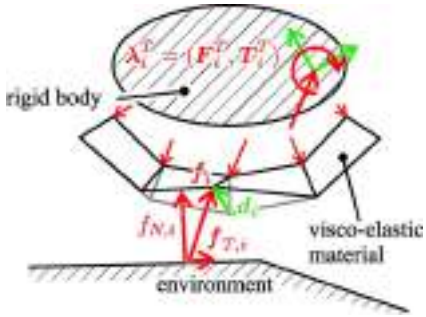

Fig. 7. Model of compliant ground contact.

with negligible mass, i.e., their dynamics are governed by

$$\boldsymbol{B}\dot{\boldsymbol{d}} + \boldsymbol{K}\boldsymbol{d} = \boldsymbol{f} \tag{4}$$

where $\boldsymbol{K}$ and $\boldsymbol{B}$ are stiffness and damping matrices, $\boldsymbol{d}$ is node displacements, and $\boldsymbol{f}$ is node forces. For diagonal $\boldsymbol{K}$ and $\boldsymbol{B}$, (4) describes decoupled point contacts, while the general case describes a linear finite-element model. The contact elements are rigidly attached to one body of the MBS, either a heel or a toe segment. Forces at the nodes attached to the MBS are summed up to the subvector $\boldsymbol{\lambda}_i$ of the full contact force vector $\boldsymbol{\lambda}^T = (\boldsymbol{\lambda}_0^T, \ldots, \boldsymbol{\lambda}_{M-1}^T)$ (Fig. 7).

Free nodes may touch the ground, but not penetrate it, i.e., there is a unilateral contact between free nodes and environment

$$f_{N,i} \geq 0 \ \wedge \ g_{N,i} \geq 0 \ \wedge \ f_{N,i} g_{N,i} = 0 \tag{5}$$

$$f_{N,i} - \mu \|\boldsymbol{f}_{T,i}\| \geq 0 \ \wedge \ (f_{N,i} - \mu \|\boldsymbol{f}_{T,i}\|) \|\dot{\boldsymbol{g}}_{T,i}\| = 0. \tag{6}$$

Here, μ is the coefficient of friction, $f_{N,i}$ and $\boldsymbol{f}_{T,i}$ are force components normal to the contact plane and in the contact plane, respectively, while $g_{N,i}$ is the minimum distance between the ith node and the environment, and $\dot{\boldsymbol{g}}_{T,i}$ is the tangential speed of the node relative to the environment.

C. Drive Dynamics

We assume a field-oriented control of the PMSM, where the magnetizing currents $\boldsymbol{I}_d = \boldsymbol{0}$ are controlled ideally and the torque producing currents $\boldsymbol{I}_q = \boldsymbol{I}$ are used for torque control. This allows a simplified modeling of the PMSM as dc motors

$$\boldsymbol{L}\dot{\boldsymbol{I}} + \boldsymbol{R}\boldsymbol{I} + \boldsymbol{k}_M \boldsymbol{\omega}_{\mathrm{rot}} = \boldsymbol{U}. \tag{7}$$

Here, $\boldsymbol{U}$ is the armature voltage, $\boldsymbol{\omega}_{\mathrm{rot}}$ the rotor's angular velocity, and $\boldsymbol{L}$, $\boldsymbol{R}$, and $\boldsymbol{k}_M$ are the inductance, resistance, and motor back electromotive force (EMF) constant, respectively. The actuator force is then given by $\boldsymbol{\tau} = \boldsymbol{k}_M \boldsymbol{I} + \boldsymbol{\tau}_{\mathrm{gear}}$, where $\boldsymbol{\tau}_{\mathrm{gear}}$ is the friction force created by reduction gears [19].

D. Time Integration

Putting all elements together, we obtain the following set of equations describing the biped robot dynamics:

$$\begin{aligned} \boldsymbol{M}\ddot{\boldsymbol{q}} + \boldsymbol{h} &= \boldsymbol{W}_{\lambda}\boldsymbol{\lambda} + \boldsymbol{W}_{\tau}\boldsymbol{\tau} \\ \boldsymbol{L}\dot{\boldsymbol{I}} + \boldsymbol{R}\boldsymbol{I} + \boldsymbol{k}_M \boldsymbol{\omega}_{\mathrm{rot}} &= \boldsymbol{U} \\ \boldsymbol{B}\dot{\boldsymbol{d}} + \boldsymbol{K}\boldsymbol{d} &= \boldsymbol{f} \end{aligned}$$

$$\begin{aligned} g_{N,i} &= \mathrm{prox}_{C_N}(f_{N,i} - r\dot{g}_{N,i}) \quad \forall i \in I_c \\ \boldsymbol{f}_{T,i} &= \mathrm{prox}_{C_T}(\boldsymbol{f}_{T,i} - r\dot{\boldsymbol{g}}_{T,i}) \quad \forall i \in I_c \end{aligned} \tag{8}$$

where $I_c = \{i | g_{N,i} = 0\}$ is the set of active contacts. The nonlinear complementarity conditions (5) and (6) were rewritten using proximal point functions [20].

The unilateral contact acts on the robot via the massless contact elements. The states therefore are strictly continuous, but their time derivatives are discontinuous making the robot is a Fillipov-type system.

We solve (4), (5), and (6) for $\boldsymbol{f}, \dot{\boldsymbol{d}}$ using a fixed point iteration scheme. Because of the discontinuity, we use a first-order method with fixed step size to calculate the time evolution of (8).

VII. Trajectory Generation

The real-time walking pattern generator calculates a trajectory for the following three steps at the beginning of each step. To facilitate real-time execution, we separate planning into smaller and simpler subtasks. First, constraints are calculated from given parameters such as average walking speed. Second, foot trajectories are planned in task space. We then calculate reference torques that minimize $\int \dot{T}_{i,\mathrm{ref}}^2 dt, i \in x, y$ and stay within the admissible range. By choosing a piecewise linear parametrization of $T_{i,\mathrm{ref}}$, we obtain a quadratic programming problem with bound constraints, that can be solved efficiently. Finally, the robot's CoM trajectory is calculated based on the previous calculation steps [21].

A. Robot Model

For real-time planning, the robot is modeled as a system of three point masses: one for each leg and a third for the body. This is a modification of the well-known *inverted pendulum model* (InvPM). Additional point masses to model swing leg dynamics have been proposed in, e.g., [22], [23].

The simplified EoM in the lateral y–z-plane is given by

$$\begin{aligned} m_b[z_b\ddot{y}_b - y_b(\ddot{z}_b + g)] \\ = -T_x + m_l \sum_{i=1..2} [y_{l,i}(\ddot{z}_{l,i} + g) - z_{l,i}\ddot{y}_{l,i}] \end{aligned} \tag{9}$$

where b denotes the body mass point, i is the foot index, and m_l is the mass of one foot mass point. In the following, we will describe the trajectory planning procedure for the lateral direction only. The procedure for the sagittal direction is identical.

Since the swing leg trajectory is calculated independently from the CoM trajectory, (9) can be written in the form of the InvPM by defining a pseudo contact torque $\tilde{T}_x := T_x - m_l \sum_{i=1..2} [y_{l,i}(\ddot{z}_{l,i} + g) - z_{l,i}\ddot{y}_{l,i}]$.

B. Problem Statement

The objective of our real-time planning system is to connect a $\mathcal{C}^2$-smooth, stable CoM trajectory for the next steps to the current trajectory. To circumvent the instabilities of (9), we avoid solving an initial value problem, and solve a boundary

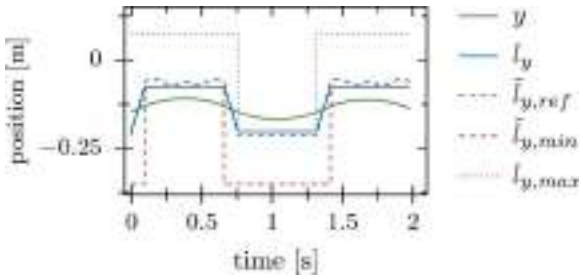

Fig. 8. Example solution using spline collocation with 30 equally spaced control points. $l_y := T_x/F_z$ is the center of pressure.

value problem (BVP) for the time interval $t \in [t_B, t_E]$ instead

$$m_b z_b \ddot{y}_b - m_b y_b(\ddot{z}_b + g) = -\tilde{T}_x \tag{10}$$

$$(y_b(t_B), \dot{y}_b(t_B), y_b(t_E))^T = (y_{b,B}, \dot{y}_{b,B}, y_{b,E})^T. \tag{11}$$

Obviously, this is an ill-posed problem, since three boundary conditions are prescribed for a second-order ODE. To obtain a well-posed problem, we modify the reference torques by adding $\gamma \Delta T_x$, where ΔT_x is a shape function, and γ the additional degree of freedom required.

C. Numerical Solution

Generally, (9) has no closed form solution, so we have implemented a collocation method with cubic splines as basis functions to numerically solve the BVP in real-time. An important property of cubic splines is their linearity in the control points $\boldsymbol{p}$, i.e., $s_i(t) = \boldsymbol{\nabla}_p s_i(t) \boldsymbol{p}$. Calculating the gradients $\boldsymbol{\nabla}_p s_i(t)$ involves solving a tridiagonal system of linear equations, which can be done very efficiently by *LR*-decomposition requiring only $O(\dim(\boldsymbol{p}))$ operations.

Putting all elements together, we have a linear set of equations in the unknown spline parameters p

$$m_b[z_{b,i} \nabla \ddot{\eta}_i - \nabla \eta_i(\ddot{z}_{b,i} + g)]\boldsymbol{p} = -\tilde{T}_{x,i} - \gamma \Delta T_{x,i} \tag{12}$$

$$\boldsymbol{p}^T (\boldsymbol{\nabla}_p \eta_0^T, \boldsymbol{\nabla}_p \dot{\eta_0}^T, \boldsymbol{\nabla}_p \eta_{n-2}^T) = (y_B, \dot{y}_B, y_E). \tag{13}$$

Here, η denotes the approximation of the solution of (10).

Fig. 8 shows a solution obtained by the proposed method for a periodic gait at 2.5 km/h using 46 cm steps and leg masses m_l of 8.2% of the robot mass. We used 30 spline parameters for three walking steps. Evidently the trajectories are smooth and the contact torques stay within the region prescribed by the sequence of support polygons.

VIII. Stabilizing Control

Due to modeling uncertainties, disturbances and an inherent instability of the walking system, on-line stabilizing control of the robot is required.

A. Related Papers

A large number of methods for stabilizing control of biped robots have been proposed. A number of similar ideas have been successfully implemented on full-size humanoid robots. Without attempting to review all methods, we briefly describe the ones we consider to be the most relevant to our approach.

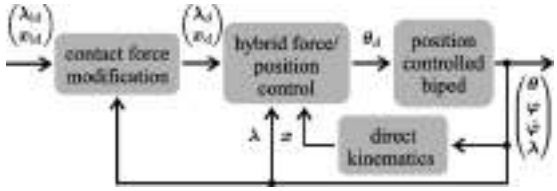

Fig. 9. Proposed walking control scheme.

A common strategy for stabilizing the upper body inclination is to control the contact torques at the feet [9], [24], [25]. Usually, the foot torques are measured by a six-axis force/torque sensor and controlled via position control of the ankle joints. Another common strategy is to accelerate the CoM [2] and [26], creating a reaction force that stabilizes the robot. In order to reduce landing impacts, many robots also incorporate an active control of vertical contact forces. This can be done by measuring the contact force and changing position set points [9], [24]. Large impacts from early foot contact have also been avoided by using low gain joint position control in combination with gain scheduling [26] or inverse dynamics feed forward control [2].

These control components are often combined in an *ad hoc* manner. However, since they are not completely orthogonal, unwanted interference is possible. Such unwanted interactions can be avoided by using an integrated control approach. Löffler proposed an approach based on feedback linearization for the biped *JOHNNIE*. Unfortunately, the performance of this method was limited by the available sensor bandwidth, computational power, model accuracy, and the difficulty performing joint torque control without joint torque sensors [9].

B. Proposed Method

We propose a generalization of the *impedance control* method previously used for *JOHNNIE* [9]. The basic idea is to use hybrid force/position control in task space with an inner joint position control loop. The contact force trajectories are modified in an outer control loop to provide inertial stabilization (Fig. 9).

The method uses a kinematic model of the robot describing the dependency of the workspace trajectories $\boldsymbol{x}$ on the generalized coordinates $\boldsymbol{q}$. The workspace trajectories include relative positions of the feet with respect to the CoM, and the orientation of the feet with respect to the upper body.

Furthermore, we introduce a simplified contact model for calculating contact forces $\boldsymbol{\lambda}$ as a function of $\boldsymbol{q}$.

1) Contact Force Modification: If the reference contact force trajectory $\boldsymbol{\lambda}_{\mathrm{id}}$ from the on-line walking pattern generator is not modified, even small perturbations will destabilize the robot. Following the idea described in Section VIII-A, desired contact forces are modified in order to stabilize global dynamics. We have chosen a potential difference (PD)-type control with saturation to obtain the modified contact torque reference $\boldsymbol{\lambda}_d$ as a function of the torso's orientation error $\boldsymbol{\Delta\varphi}_{\mathrm{torso}}$

$$\boldsymbol{\lambda}_{\mathrm{d}} = \mathrm{sat}(\boldsymbol{\lambda}_{\mathrm{id}} + \boldsymbol{K}_P \boldsymbol{\Delta\varphi}_{\mathrm{torso}} + \boldsymbol{K}_D \boldsymbol{\Delta\dot{\varphi}}_{\mathrm{torso}}). \tag{14}$$

The orientation $\boldsymbol{\varphi}_{\mathrm{torso}}$ is expressed by the rotation about the gravity vector φ_z, and the relative angles φ_x, φ_y between the

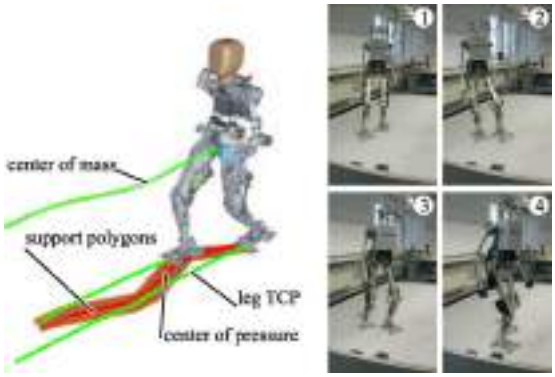

Fig. 10. Simulation of *LOLA* and walking experiment with *JOHNNIE*, both using the proposed control system.

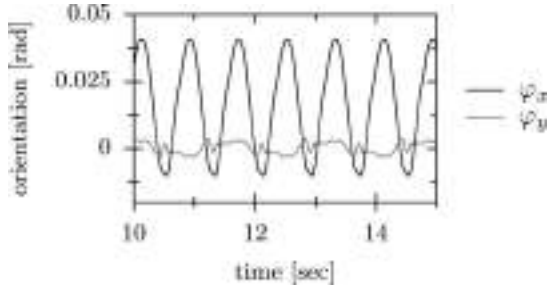

Fig. 11. Simulated upper body orientation for *LOLA* walking in a straight line (φ_x in sagittal, φ_y in lateral plane).

torso's vertical axis and the gravity vector in the sagittal and lateral planes, respectively. $\boldsymbol{K}_P$ and $\boldsymbol{K}_D$ are gain matrices and sat is a saturation function that returns only physically feasible contact forces. The control gains are scheduled to follow changing load factors during different walking phases and to distribute the contact forces between left and right leg during double support.

2) Contact Model: The foot ground contact is modeled as a set of decoupled point contacts with stiffness $\boldsymbol{C}_i$ and negligible damping. Using the known contact state, i.e., which contacts are opened or closed, the total force $\boldsymbol{F}_j$ and torque $\boldsymbol{T}_j$ acting on foot j are given by

$$\begin{pmatrix} \boldsymbol{F}_j \\ \boldsymbol{T}_j \end{pmatrix} = \sum_{i \in I_{c,j}} \begin{pmatrix} {}_j\boldsymbol{C}_i \boldsymbol{d}_{c,i} \\ {}_j\boldsymbol{\Delta r}_{c,i} \times {}_j\boldsymbol{C}_i \boldsymbol{d}_{c,i} \end{pmatrix} \tag{15}$$

where $I_{c,j}$ denotes the subset of I_c on foot j, $\boldsymbol{d}_{c,i}$ is the deformation of the ith contact element and ${}_j\boldsymbol{\Delta r}_{c,i}$ is the vector from the force sensor frame to the contact element.

3) Control Law: The subset of contact forces $\boldsymbol{\lambda}_c$ to be actively controlled is set in a selection matrix $\boldsymbol{S}_\lambda$. We also select a subspace $\boldsymbol{x}_c = \boldsymbol{S}_x \boldsymbol{x}$ to be position controlled using a second matrix $\boldsymbol{S}_x$. The use of selection matrices is similar to the use of a selection vector proposed by Craig and Raibert [27] to choose position and force controlled dimensions in task space. The major difference lies in the fact that we have separate selection matrices for contact forces and task space dimensions, i.e., the selection of force- and position-controlled dimensions does not have to be carried out in the same coordinate system and the robot may be redundant.

In the nonposition-controlled dimensions, we allow a modification of the reference trajectories $\boldsymbol{\Delta x}_\lambda$ for force control. With $\boldsymbol{K}_\lambda$ as a control gain, we choose the linear error dynamics

$$\boldsymbol{S}_\lambda \left(\boldsymbol{\Delta \dot{\lambda}} + \boldsymbol{K}_\lambda \boldsymbol{\Delta \lambda} \right) = 0. \tag{16}$$

With $\bar{\boldsymbol{S}}_x$ denoting the complement of $\boldsymbol{S}_x$, we have

$$\boldsymbol{\Delta \dot{x}}_\lambda = \bar{\boldsymbol{S}}_x \boldsymbol{\nabla}_q \boldsymbol{x} \boldsymbol{\Delta \dot{q}}. \tag{17}$$

Using the least squares solution for $\boldsymbol{\Delta \dot{q}}$ and $\dot{\boldsymbol{\lambda}} = \boldsymbol{\nabla}_q \boldsymbol{\lambda} \dot{\boldsymbol{q}}$, we obtain the following reference trajectory modification:

$$\boldsymbol{\Delta \dot{x}}_\lambda = (\boldsymbol{S}_\lambda \boldsymbol{\nabla}_q \boldsymbol{\lambda} \left(\bar{\boldsymbol{S}}_x \boldsymbol{\nabla}_q \boldsymbol{x} \right)^{\#})^{\#} \boldsymbol{S}_\lambda \left(\dot{\boldsymbol{\lambda}}_d + \boldsymbol{K}_\lambda (\boldsymbol{\lambda}_d - \boldsymbol{\lambda}) \right)$$

where $(\cdot)^{\#}$ denotes the Moore–Penrose pseudoinverse. $\boldsymbol{\nabla}_q \boldsymbol{\lambda}$ is calculated from (14) and will approach zero for the swing leg, therefore, (17) is modified to include a position control term

$$\begin{aligned} \boldsymbol{\Delta \dot{x}}_\lambda = \boldsymbol{\alpha}_\lambda \{ \left[\boldsymbol{S}_\lambda \boldsymbol{\nabla}_q \boldsymbol{\lambda} (\bar{\boldsymbol{S}}_x \boldsymbol{\nabla}_q \boldsymbol{x})^{\#} \right]^{\#} \boldsymbol{S}_\lambda \left[\boldsymbol{K}_{\lambda,\mathrm{ff}} \dot{\boldsymbol{\lambda}}_d \right. \\ \left. + \boldsymbol{K}_\lambda (\boldsymbol{\lambda}_d - \boldsymbol{\lambda}) \right] \} + \boldsymbol{\alpha}_x \left[\bar{\boldsymbol{S}}_x \boldsymbol{K}_{\lambda x} (\boldsymbol{x}_d - \boldsymbol{x}) \right]. \end{aligned} \tag{18}$$

Here, $\boldsymbol{\alpha}_\lambda$ and $\boldsymbol{\alpha}_x$ are gain matrices and $\boldsymbol{\alpha}_\lambda + \boldsymbol{\alpha}_x = \boldsymbol{E}$ is the unity matrix. The gain $\boldsymbol{K}_{\lambda,\mathrm{ff}}$ modifies the feed-forward term $\dot{\boldsymbol{\lambda}}_d$ and is tuned during walking experiments. The force control gain $\boldsymbol{\alpha}_\lambda$ is zero for the swing leg, avoiding instability due to a vanishing contact stiffness and allowing the position control term to move the swing leg back toward the reference trajectory.

To obtain a position control reference on joint level, the task space reference modified according to (18) must be mapped into joint space. For this we use a resolved motion rate control scheme [28] with nullspace optimization [29]

$$\begin{aligned} \dot{\boldsymbol{x}}_d &= \dot{\boldsymbol{x}}_{\mathrm{id}} + \bar{\boldsymbol{S}}_x^T \boldsymbol{\Delta \dot{x}}_\lambda + \frac{\boldsymbol{K}_x}{\Delta t} \left\{ \boldsymbol{x}_{\mathrm{id}} + \bar{\boldsymbol{S}}_x^T \boldsymbol{\Delta x}_\lambda - \boldsymbol{x} \right\} \\ \boldsymbol{\Delta x}_\lambda &= \int \boldsymbol{\Delta \dot{x}}_\lambda dt \\ \dot{\boldsymbol{q}} &= (\boldsymbol{\nabla}_q \boldsymbol{x})^{\#} \dot{\boldsymbol{x}} - \alpha_N \boldsymbol{N} \boldsymbol{\nabla}_q H. \end{aligned} \tag{19}$$

Here, $\boldsymbol{N}$ is the nullspace projection matrix and α_N a gain for minimizing the objective function H in $\boldsymbol{x}$'s nullspace. Currently, we use two components for H: joint limit avoidance and convergence to a "comfortable" pose. Joint limit avoidance is only activated in a boundary close to the joint limits and deactivated otherwise. For convergence toward a "comfortable" pose, we use a quadratic cost function that penalizes divergence from a reference pose according to each joint's range of motion. The control method is described in more detail in [30].

Fig. 10 shows snapshots of walking experiments with *JOHNNIE* and a simulation of *LOLA* using the proposed planning and control algorithms. An example of an IMU signal for *LOLA* walking in our dynamics simulation is shown in Fig. 11.

IX. Conclusion

Humanoid robots are a new and promising application area for robotics. In order to be useful and commercially successful, humanoids must have reliable biped locomotion capabilities. In this paper, we focused on aspects of the mechatronic

hardware design and real-time control system of our new biped robot *LOLA*. Its distributed electronics architecture, revised sensor system, brushless motors, and extremely lightweight design significantly improve the physical capabilities. New trajectory planning and control algorithms to improve walking capabilities were developed and extensively tested both in dynamics simulations and in walking experiments with *JOHNNIE*. *LOLA* has been fully assembled, and we are currently performing initial experiments.

ACKNOWLEDGMENT

The authors would like to extend sincere thanks to M. Bachmayer, V. Favot, G. Mayr, and M. Schwienbacher for their contributions to the *LOLA* project. The authors would also like to thank the reviewers for their helpful comments.

REFERENCES

[1] IFR Statistical Department. (2008). *World robotics* [Online]. Available: http://www.worldrobotics.org/

[2] D. Tajima, R. Honda, and K. Suga, "Fast running experiments involving a humanoid robot," in *Proc. IEEE Int. Conf. Robot. Autom. (ICRA)*, 2009, pp. 1571–1576.

[3] M. Hirose and K. Ogawa, "Honda humanoid robots development," *Philos. Trans. R. Soc. A*, vol. 365, pp. 11–19, 2007.

[4] K. Nishiwaki, J. Kuffner, S. Kagami, M. Inaba, and H. Inoue, "The experimental humanoid robot H7: A research platform for autonomous behaviour," *Philos. Trans. R. Soc. A*, vol. 365, no. 1850, pp. 79–107, 2007.

[5] K. Kaneko, F. Kanehiro, S. Kajita, H. Hirukawa, T. Kawasaki, M. Hirata, K. Akachi, and T. Isozumi, "Humanoid robot HRP-2," in *Proc. IEEE Int. Conf. Robot. Autom. (ICRA)*, 2004, pp. 1083–1090.

[6] K. Kaneko, K. Harada, F. Kanehiro, G. Miyamori, and K. Akachi, "Humanoid robot HRP-3," in *Proc. IEEE/RSJ Int. Conf. Intell. Robots Syst. (IROS)*, 2008, pp. 2471–2478.

[7] Y. Ogura, H. Aikawa, K. Shimomura, H. Kondo, A. Morishima, H. Lim, and A. Takanishi, "Development of a humanoid robot WABIAN-2," in *Proc. IEEE Int. Conf. Robot. Autom. (ICRA)*, 2006, pp. 76–81.

[8] J.-Y. Kim, I.-W. Park, J. Lee, M.-S. Kim, B.-K. Cho, and J.-H. Oh, "System design and dynamic walking of humanoid robot KHR-2," in *Proc. IEEE Int. Conf. Robot. Autom. (ICRA)*, 2005, pp. 1443–1448.

[9] K. Löffler, M. Gienger, F. Pfeiffer, and H. Ulbrich, "Sensors and control concept of a biped robot," *IEEE Trans. Ind. Electron.*, vol. 51, no. 5, pp. 972–80, Oct. 2004.

[10] S. Kajita, T. Nagasaki, K. Kaneko, K. Yokoi, and K. Tanie, "A hop towards running humanoid biped," in *Proc. IEEE Int. Conf. Robot. Autom. (ICRA)*, 2004, pp. 629–635.

[11] D. Kerrigan, U. Croce, M. Marciello, and P. Riley, "A refined view of the determinants of gait: Significance of heel rise," *Arch. Phys. Med. Rehabil.*, vol. 81, pp. 1077–1080, 2000.

[12] K. Nishiwaki, S. Kagami, Y. Kuniyoshi, M. Inaba, and H. Inoue, "Toe joints that enhance bipedal and fullbody motion of humanoid robots," in *Proc. IEEE Int. Conf. Robot. Autom. (ICRA)*, 2002, pp. 3105–3110.

[13] *Design Methodology for Mechatronic Systems*, VDI Std. 2206, Jun. 2004.

[14] S. Kajita and K. Tani, "Experimental study of biped dynamic walking in the linear inverted pendulum mode," in *Proc. IEEE Int. Conf. Robot. Autom. (ICRA)*, 1995, pp. 2885–2891.

[15] S. Lohmeier, T. Buschmann, M. Schwienbacher, H. Ulbrich, and F. Pfeiffer, "Leg design for a humanoid walking robot," in *Proc. IEEE-RAS Int. Conf. Humanoid Robot. (Humanoids)*, 2006, pp. 536–541.

[16] S. Lohmeier, T. Buschmann, H. Ulbrich, and F. Pfeiffer, "Modular joint design for performance enhanced humanoid robot LOLA," in *Proc. IEEE Int. Conf. Robot. Autom. (ICRA)*, 2006, pp. 88–93.

[17] J. Perry, *Gait Analysis—Normal and Pathological Function*, 3rd ed. Thorofare, NJ: Slack, 1992.

[18] J. Bevans, "Biomechanics: A review of foot function in gait," *Foot*, vol. 2, no. 2, pp. 79–82, 1992.

[19] T. Buschmann, S. Lohmeier, H. Ulbrich, and F. Pfeiffer, "Dynamics simulation for a biped robot: Modeling and experimental verification," in *Proc. IEEE Int. Conf. Robot. Autom. (ICRA)*, 2006, pp. 2673–2678.

[20] R. Rockafellar, "Augmented lagrangians and applications of the proximal point algorithm in convex programming," *Math. Oper. Res.*, vol. 1, no. 2, pp. 97–116, 1976.

[21] T. Buschmann, S. Lohmeier, M. Bachmayer, H. Ulbrich, and F. Pfeiffer, "A collocation method for real-time walking pattern generation," in *Proc. IEEE-RAS Int. Conf. Humanoid Robot. (Humanoids)*, 2007, pp. 1–6.

[22] T. Takenaka, "Gait generation system of legged mobile robot," Eur. Patent 1 671 754-A2, Jun. 21, 2006.

[23] J. Park and K. Kim, "Biped robot walking using gravity-compensated inverted pendulum mode and computed torque control," in *Proc. IEEE Int. Conf. Robot. Autom. (ICRA)*, 1998, pp. 3528–3533.

[24] S. Kajita, T. Nagasaki, K. Kaneko, K. Yokoi, and K. Tanie, "A running controller of humanoid biped HRP-2LR," in *Proc. IEEE Int. Conf. Robot. Autom. (ICRA)*, 2005, pp. 616–622.

[25] T. Takenaka, "Controller of legged mobile robot," Eur. Patent 1 475 198-A1, Nov. 10, 2004.

[26] K. Nishiwaki, "Design of walking system and online control of a humanoid robot," Ph.D. dissertation, University of Tokyo, Tokyo, Japan, 2001.

[27] J. Craig and M. Raibert, "A systematic method of hybrid position/force control of a manipulator," in *Proc. Comput. Softw. Appl. Conf., IEEE Comput. Soc.*, 1979, pp. 446–451.

[28] D. E. Whitney, "Resolved motion rate control of manipulators and human prostheses," *IEEE Trans. Man Mach. Syst.*, vol. MMS-10, no. 2, pp. 47–53, Jun. 1969.

[29] A. Liégeois, "Automatic supervisory control of the configuration and behavior of multibody mechanisms," *IEEE Int. Trans. Syst., Man, Cybern.*, vol. SMC-7, no. 12, pp. 63–71, Dec. 1977.

[30] T. Buschmann, S. Lohmeier, and H. Ulbrich, "Biped walking control based on hybrid position/force control," in *Proc. IEEE/RSJ Int. Conf. Intell. Robots Syst. (IROS)*, 2009.

Sebastian Lohmeier received the Diploma degree in mechanical engineering from the Technical University Munich, Garching, Germany, in 2003. He is currently working toward the Ph.D. degree at the Institute of Applied Mechanics, Technical University Munich.

He is a Research Assistant at the Institute of Applied Mechanics, Technical University Munich, where he has been engaged in the design and realization of the biped robot *LOLA*'s mechatronic system. His research interests include humanoid robotics, mechatronic systems, actuators, and sensors.

Thomas Buschmann received the Diploma degree in mechanical engineering from the Technical University Munich, Garching, Germany, in 2003. He is currently working toward the Ph.D. degree at the Institute of Applied Mechanics, Technical University Munich, where he has been engaged in the simulation and control of the biped robots *JOHNNIE* and *LOLA*.

His research interests include walking robots, multibody dynamics, and control.

Heinz Ulbrich received the Ph.D. degree and the Habilitation from the Technical University Munich, Garching, Germany, in 1979 and 1986, respectively.

From 1979 to 1988, he was Chief Engineer at the Technical University Munich. After one year as Senior Research Fellow at the NASA Lewis Research Center, Cleveland, OH, he joined the Technical University Braunschweig as a Professor. He was a Professor at Essen University, Essen, Germany, during 1994. Since 2001, he has been the Head of the Institute of Applied Mechanics, Technical University Munich. His current research interests include modeling, simulation, control, and realization of mechatronic systems.